Combining Steady-State Accuracy and Responsiveness of PMU Estimates: An Approach Based on Left and Right Taylor–Fourier Expansions

Guglielmo Frigo, *Senior Member, IEEE*, Giacomo Gallus, *Graduate Student Member, IEEE*, Paolo Attilio Pegoraro, *Senior Member, IEEE*, and Sergio Toscani, *Senior Member, IEEE*

***Abstract*— Modern power systems are characterized by fast dynamics, due to the massive presence of power electronics-based converters. In this scenario, the present article proposes an approach for measuring synchrophasor, frequency, and rate of change in frequency (ROCOF) that allows to effectively cope with abrupt transients. The method is based on Taylor–Fourier models, which typically consider an observation interval centered on the reporting instant. In this article, the Taylor expansion is performed on asymmetric windows, which look either at the left or at the right of the measurement instant. A reconstruction algorithm enables a seamless blend between left and right estimates that, while preserving accuracy during steady-state or slowly varying conditions, leads to an exemplary behavior in amplitude and phase step tests, also in the presence of wideband noise. In particular, an M-class compliant estimator is designed to highlight the potentialities of the proposed approach. Zero synchrophasor, frequency, and ROCOF response times are obtained, since steady-state accuracy limits are never exceeded in the presence of step variations. From a different point of view, the proposed technique does not return invalid estimates, thus it is capable of also tracking abrupt transitions.**

***Index Terms*— Amplitude step, phase step, phasor measurement unit (PMU), response time (RT), Taylor–Fourier (TF) expansion, TF multifrequency (TFM).**

Manuscript received 28 February 2024; accepted 24 March 2024. Date of publication 3 April 2024; date of current version 17 April 2024. The work of Guglielmo Frigo was supported by the Swiss Federal Office of Energy through QUINPORTION Research Program under Grant SI/502415. The work of Paolo Attilio Pegoraro was supported by Italian Ministerial Grant PRIN 2022 "Smart Grid-Connected Power Converters Based on Advanced Synchrophasor-Inspired Harmonics Measurements for Holistic Integration of Renewable Energy Sources (POWERHERO)" under Grant 20224X2AYH and Grant CUP F53D23000490006. The work of Sergio Toscani was supported by Italian Ministerial Grant PRIN 2022 "Next-Generation Distributed Synchronized Measurement Systems for Smart Grids With Self-Diagnostics Capabilities and Self-Improvement of Information Quality" under Grant 2022RYZJT9 and Grant CUP D53D23001470006. The Associate Editor coordinating the review process was Dr. Yau Chung. *(Corresponding author: Guglielmo Frigo.)*

Guglielmo Frigo is with the Electrical Energy and Power Laboratory, Swiss Federal Institute of Metrology, 3084 Bern-Wabern, Switzerland (e-mail: guglielmo.frigo@metas.ch).

Giacomo Gallus and Paolo Attilio Pegoraro are with the Department of Electrical and Electronic Engineering of the University of Cagliari, 09123 Cagliari, Italy (e-mail: giacomo.gallus@unica.it; paolo.pegoraro@unica.it).

Sergio Toscani is with the Dipartimento di Elettronica, Informazione e Bioingegneria, Politecnico di Milano, 20133 Milan, Italy (e-mail: sergio.toscani@polimi.it).

Digital Object Identifier 10.1109/TIM.2024.3384553

I. Introduction

In RECENT years, power systems are experiencing a rapid and significant transformation due to the integration of renewable energy sources [1]. Such resources are typically connected via dedicated power converters that do not contribute to the overall system inertia [2]. The consequence is that power systems are more prone to highly dynamic conditions, as proven by the recent contingencies occurred in California [3] and Australia [4].

In this context, a distributed measurement infrastructure is the backbone of any monitoring and control application [5], [6]. Phasor measurement units (PMUs) represent a promising solution, thanks to their capability of providing accurate estimates with update rates in the order of tens of frames per second (fps). In this regard, the reference standard—IEC/IEEE 60255-118-1, briefly PMU Std [7]—introduces two performance classes (P and M) and the corresponding requirements in terms of estimation accuracy, response time (RT), and reporting latency.

It is worth noting that the PMU Std was originally conceived for transmission systems networks, characterized by slowly changing operating conditions and low waveform distortion. In accordance with this assumption, the PMU Std prescribes accuracy requirements that are significantly relaxed in the presence of dynamics or transients.

The new operating scenario, though, is pushing for the development of enhanced PMUs, capable of optimizing at the same time estimation accuracy, reporting latency and RT. Examples of different approaches and research directions can be found, for instance, in [8], [9], [10], and [11].

A still open issue is represented by PMU response to step changes in magnitude and phase [12] that can be interpreted as sudden transitions between two steady-state conditions. Such discontinuities can be hardly represented with slowly modulated sinusoidal signal models, which are those traditionally used in many PMUs [13]. A possible solution consists in applying a step detection technique and adapting the estimation algorithm accordingly [14]. This approach was also adopted in [15] to switch between a P-class and an M-class measurement channel and in [16] to define an algorithm that is simultaneously compliant with classes P and M.

By means of the Hilbert transform (HT), it is possible to define the underlying analytic signal and check either its

envelope, like in [17] and [18] where reference step location is intended for calibration purposes, or its spectrum [19]. An alternative solution relies on the use of dictionaries of predefined set of waveforms, either inspired by the PMU Std test conditions [20] or by suitably modified wavelet functions [21].

However, both these solutions suffer from different shortcomings. The first one requires a precise and effective method for the computation of the analytic signal associated with the considered window [22]. The second one is computationally demanding (i.e., not easily implementable in real-time applications) and depends on the dictionary granularity [23].

For these reasons, in this article we focus on a promising PMU estimation algorithm that, depending on the configuration, has been proven to be compliant with P- and M-class requirements, and we try to improve its performance during fast transients. More precisely, we consider a Taylor–Fourier multifrequency (TFM) model [24] that includes the fundamental component and its first four harmonic terms. This solution represents an extension of the Taylor–Fourier filters (TFFs) introduced in [25], where it was proposed to track the fundamental component oscillations. By properly setting the expansion degrees, a bank of TFFs can also be used to promptly detect and classify fault events [26].

Instead of applying the TFM on the entire window, which is symmetric with respect to the reporting instant, in [27] the authors investigated the possibility of limiting the TFM expansion only to a portion. Based on a simple yet effective discontinuity detection algorithm, which allows for choosing the best part (left-half, right-half, or full window) for the TFM expansion, a P-class compliant algorithm was proposed with the target of minimizing estimation errors during transients, featuring zero phasor measurement RT during magnitude and phase-angle steps as those prescribed by the PMU Std.

In this article, which is a technical extension of [27], the algorithm is generalized to also address the design of algorithms with better measurement and noise-rejection performance, as those M-class compliant, which rely on longer windows, usually resulting in slower step responses. The main contribution is to provide, even for this scenario, zero or quasi-zero RTs during abrupt changes, thanks to a measurement-oriented fusion of the estimates obtained with the left and right TFM expansions. The aim is to propose a solution for synchrophasor, frequency, and rate of change of frequency (ROCOF) measurements that is both accurate in steady-state conditions and under slow dynamics, and remarkably prompt to react to transients. It is important to highlight that the proposal is intended to reduce the number of "invalid" measurements, i.e., measurements affected by large errors that must be discarded, since they may lead to misleading results when used in any application. Indeed, many methods, even though compliant with the PMU Std, give, around abrupt transients, large intervals of inaccurate and even nonmetrologically sound measured values, which can be avoided or limited by adopting the presented idea.

This article is organized as follows. Section II presents the main principles of TFM models for PMUs. In Section III, we introduce the proposed method. Section IV shows the performance of the proposed method and illustrates a qualitative and quantitative comparison with other state-of-art methods. Finally, in Section V, we provide some closing remarks.

II. TF Models for PMU Algorithms

Let us consider an electric signal $x(t)$ in an ac power system having rated frequency f_0, corresponding to the angular frequency ω_0. Typically, whatever method is considered, $x(t)$ is assumed to be generated as the projection on the real axis of a complex-valued function having slowly varying magnitude (when compared to f_0), whose angular speed in the complex plane is close to ω_0. In terms of equations, we have

$$x(t) = \sqrt{2}\Re\left\{\bar{X}_0(t)e^{j\omega_0 t}\right\} + d(t) \tag{1}$$

where $\bar{X}_0(t)$ is the synchrophasor (overline denotes complex-valued quantities), while frequency deviation and ROCOF are obtained straightforwardly from the first- and second-order derivatives of $\angle\bar{X}_0(t)$. The term $d(t)$ embeds all the residual signal contributions, e.g., wideband noise and other spectral components; typically $|d(t)| \ll |\bar{X}_0(t)|$.

An important class of estimation methods relies on a TF model of the signal [25], [28]. Let us suppose that measurements should be performed in $t = t_r$, which is the measurement or reporting instant. In this case, $M = 2N + 1$ samples in an observation window having length $T_w = MT_s$ and centered on t_r are expressed through the Taylor expansions of the real and imaginary parts of the synchrophasor around t_r, truncated to the K_0th degree. Using matrix notation, the M-size vector of the samples (collected with sampling interval T_s) is written as

$$\mathbf{x}(t_r) = \begin{bmatrix} x(t_r + NT_s) \\ \vdots \\ x(t_r) \\ \vdots \\ x(t_r - NT_s) \end{bmatrix} = \bar{\mathbf{B}}\bar{\mathbf{p}}(t_r) + \mathbf{r}(t_r) \tag{2}$$

having introduced the M-size residual vector $\mathbf{r}(t_r)$ and the $(2K_0 + 2)$-size vector of the model parameters

$$\bar{\mathbf{p}}(t_r) = \left[\bar{X}_0^{(0)}(t_r) \cdots \bar{X}_0^{(K_0)}(t_r) \;\; \underline{X}_0^{(0)}(t_r) \cdots \underline{X}_0^{(K_0)}(t_r)\right]^{\mathsf{T}} \tag{3}$$

where $\bar{X}_0^{(k)}$ is the kth-order derivative of the synchrophasor (and $\bar{X}_0^{(0)} = \bar{X}_0$), while underline indicates complex conjugation. All these parameters refer to the instant t_r, even if from here on it will often be omitted for the sake of brevity. The $M \times (2K_0 + 2)$ matrix $\bar{\mathbf{B}}$ can be partitioned as

$$\bar{\mathbf{B}} = \left[\bar{\mathbf{\Phi}}(\omega_0)\mathbf{A}(K_0) \;\; \underline{\mathbf{\Phi}}(\omega_0)\mathbf{A}(K_0)\right] \tag{4}$$

where

$$\bar{\mathbf{\Phi}}(\omega) = \mathrm{diag}\left[e^{j\omega NT_s} \cdots e^{-j\omega NT_s}\right]e^{j\omega t_r} \tag{5}$$

is the $M \times M$ phase rotation matrix, while

$$\mathbf{A}(K) = \frac{\sqrt{2}}{2}\begin{bmatrix} 1 & NT_s & \frac{(NT_s)^2}{2} & \cdots & \frac{(NT_s)^K}{K!} \\ \vdots & \vdots & \vdots & & \vdots \\ 1 & 0 & 0 & & 0 \\ \vdots & \vdots & \vdots & & \vdots \\ 1 & -NT_s & \frac{(-NT_s)^2}{2} & \cdots & \frac{(-NT_s)^K}{K!} \end{bmatrix} \tag{6}$$

is an $M \times (K+1)$ matrix.

An estimate $\hat{\bar{\mathbf{p}}}(t_r)$ of the TF model parameters can be obtained by minimizing the Euclidean norm of the misfit, namely, the deviation between the samples in the current time window and their reconstructions obtained from the model. If the number of parameters defining the TF model (namely, $2(K_0+1)$) is lower than M, the optimization problem can be solved in the least squares (LS) sense by computing $\bar{\mathbf{H}} = \bar{\mathbf{B}}^{\dagger}$, with † denoting the Moore–Penrose inverse. The mth element of $\hat{\bar{\mathbf{p}}}$ is obtained by convolving the samples with the mth row of $\bar{\mathbf{H}}$, and thus, its elements correspond to the (complex-valued) coefficients of an FIR filter, often known as TFF [25]. If $K_0 \geq 2$, the estimates of the synchrophasor, frequency, and ROCOF in t_r can be obtained from the first three components of $\hat{\bar{\mathbf{p}}}(t_r)$, i.e., $\{\hat{\bar{X}}_0^{(k)}\}_{k\in\{0,1,2\}}$.

The quality of the estimates strongly depends on how well the adopted TF model is able to match the actual signal in the considered observation interval. In particular, the estimate is exact if the signal in the observed time window belongs to the subspace spanned by the selected TF model, thus implying that $\mathbf{x}(t_r)$ can be expressed as a linear combination of the columns of $\bar{\mathbf{B}}$.

However, in practical situations, the model is not exact, and therefore, $\mathbf{x}(t_r)$ is outside the subspace generated by the columns of $\bar{\mathbf{B}}$. Under these conditions, it is beneficial to favor a smaller residual in the neighborhood of the measurement instant t_r, at the expense of a worse fitting near the edges of the samples record. For this purpose, it is possible to introduce a weighting vector $\mathbf{w}$ (see [29], [30] for TFFs, and [31] for TFM, which is better discussed in what follows) while minimizing the Euclidean norm of the weighted residual $\mathbf{r}_w(t_r) = \mathbf{W}\mathbf{r}(t_r)$, with $\mathbf{W} = \mathrm{diag}(\mathbf{w})$. From a mathematical point of view, it corresponds to a weighted LS (WLS) problem, i.e., a minimization of the residuals norm, which can be written as

$$\hat{\bar{\mathbf{p}}}(t_r) = \arg\min_{\bar{\mathbf{p}}} \|\bar{\mathbf{B}}_w\bar{\mathbf{p}} - \mathbf{x}_w(t_r)\| \tag{7}$$

where

$$\bar{\mathbf{B}}_w = \mathbf{W}\bar{\mathbf{B}} \quad \mathbf{x}_w(t_r) = \mathbf{W}\mathbf{x}(t_r). \tag{8}$$

The solution of (7) results as

$$\hat{\bar{\mathbf{p}}}(t_r) = \bar{\mathbf{B}}_w^{\dagger}\mathbf{x}_w(t_r) = \bar{\mathbf{H}}_w\mathbf{x}(t_r) \tag{9}$$

with $\bar{\mathbf{H}}_w$ defining a new bank of TFFs, generally having wider passbands because of the introduction of weighting.

The above-described TFFs can also be designed starting from a different reference frequency $\omega \neq \omega_0$ using seamlessly (5), (6), and $\mathbf{w}$ to build a new $\bar{\mathbf{B}}_w(\omega)$ and, as a consequence, a new $\bar{\mathbf{H}}_w(\omega)$ to solve the estimation problem. This results in a frequency shift of both passband and zeros of TFFs.

When looking at (1), the presence of significant narrowband components (such as harmonics) in the term $d(t)$ generates mismatch between the signal and TF model. Under these conditions, the WLS solution (9) is not able to effectively separate the signal from the disturbance subspace; the result is that the obtained estimates are affected by the presence of $d(t)$, and thus, accuracy is degraded.

A possible solution to overcome this problem is enlarging the signal model subspace to include the most relevant narrowband components, whose spectral content is located around each frequency in the set $\{\omega_q\}_{q\in\{1,\ldots,Q\}}$. Their interference on fundamental synchrophasor, frequency, and ROCOF estimates is thus dramatically mitigated. From an implementation point of view, thanks to the narrowband assumption, the signal contribution coming from the generic qth disturbance can be written through a Taylor expansion of the corresponding synchrophasor around t_r, truncated to the K_qth degree. This leads to the so-called TFM models [24], which can be expressed in the form (2), but now

$$\bar{\mathbf{p}} = \left[\bar{\mathbf{p}}_0^{\intercal} \;\; \bar{\mathbf{p}}_1^{\intercal} \cdots \bar{\mathbf{p}}_Q^{\intercal}\right]^{\intercal} \tag{10}$$

with

$$\begin{aligned} \bar{\mathbf{p}}_q &= \left[\bar{X}_q^{(0)} \cdots \bar{X}_q^{(K_q)} \;\; \underline{X}_q^{(0)} \cdots \underline{X}_q^{(K_q)}\right]^{\intercal} \\ \bar{\mathbf{B}} &= \left[\bar{\mathbf{\Phi}}(\omega_0)\mathbf{A}(K_0) \;\; \underline{\mathbf{\Phi}}(\omega_0)\mathbf{A}(K_0) \cdots \underline{\mathbf{\Phi}}(\omega_Q)\mathbf{A}(K_Q)\right]^{\intercal}. \end{aligned} \tag{11}$$

The spectral components to be embedded in the signal model (namely, its spectral support) can be either retrieved through an iterative procedure or they can be included *ex-ante*. In this respect, significant low-order harmonics are often present in power system waveforms, and they may have notable impact on the estimates. For this reason, the adopted TFM model often considers components whose frequencies are the first multiples of f_0.

III. Proposed Method

PMU algorithms based on TFM models assume that the time evolutions of the magnitude and phase angle of the fundamental term are smooth. Under this condition, given the typical length of the observation window (bounded by the maximum latency constraint), the fundamental component can be accurately tracked with K_0 typically equal to 2 or 3 (see, for instance, [11], [16], [25]). As mentioned above, $K_0 \geq 2$ is needed to compute the first- and second-order derivatives of the phase angle. Higher expansion degrees are not generally adopted: on one hand, measurement bandwidth is increased, but on the other hand estimates become more prone to spectral interference from both the narrowband components and wideband noise. In some cases, this drawback can outweigh the potential advantage.

During faults, switching, or in case of sudden load variations, voltage and current waveforms may exhibit an abrupt transition between two different steady-state conditions, which could be idealized as a step-like change in magnitude or phase of the underlying phasor. To asses performance in the presence of such events, the PMU Std prescribes compliance

tests where the applied sinusoidal signal at nominal frequency contains jumps either in amplitude or in phase; let us assume that a step occurs in the time instant t_{step}. When $t_r < t_{\text{step}}$, an ideal PMU algorithm should return the synchrophasor value corresponding to the steady-state before the step, zero frequency deviation (with respect to the nominal value), and zero ROCOF; when $t_r > t_{\text{step}}$, the measured synchrophasor should switch to the steady-state value after the step change, while frequency deviation and ROCOF should remain zero.

In general, this does not happen with real-world PMU algorithms: the relationship between input samples and measurements is dynamic, hence it unavoidably slows down the transition between the two steady-state conditions. For example, in case of PMU methods based on FIR filtering, the duration of the transition corresponds to the length of the filter. The PMU Std quantifies this phenomenon in terms of RT, defined as the duration of the time interval across the step event where steady-state accuracy limits for synchrophasor, frequency, and ROCOF measurements are violated.

A. Left and Right TF Estimates

It is immediately evident that a TFM model of the observed samples does not represent an effective tool to deal with step changes, just as a Taylor expansion struggles in approximating discontinuities. As previously pointed out, improving responsiveness by enlarging the bandwidth of the TFFs (namely, increasing the Taylor expansion degree or adopting proper weights) is not a good choice. Therefore, different approaches should be developed to enhance performance of TFM-based PMU algorithms during step variations.

From a different point of view, the reporting instant splits the $2N+1$ sample window into two $N+1$ sample subwindows: one located at the left and the other at the right of t_r (both of them include the sample in t_r). In the presence of a step within the full window, if $t_r < t_{\text{step}}$, the left subwindow does not contain the step, and all its samples are related to the steady-state condition before the step. Conversely, when $t_r > t_{\text{step}}$, the right subwindow does not include the step event, while the corresponding samples are tied to the steady-state after the step. Therefore, if one were able to perform measurements using just the left subwindow for $t_r < t_{\text{step}}$, while switching to the right subwindow as t_r exceeds t_{step}, it would be possible to approach the ideal behavior in the presence of step changes.

The starting point of the idea is having available a method that enables obtaining the measurements in t_r by processing just the samples in either the left or right subwindow. A possible solution is adopting the TFM approach, but considering asymmetric expansions of the embedded components, looking exclusively at the left or right of t_r. Let us first define the left and right subwindows $\mathbf{x}_{\text{L}}(t_r)$ and $\mathbf{x}_{\text{R}}(t_r)$, corresponding to the last and first $N+1$ components of $\mathbf{x}_w(t_r)$, respectively. The left and right TFM models can be written as

$$\mathbf{x}_S(t_r) = \bar{\mathbf{B}}_S \bar{\mathbf{p}}_S(t_r) + \mathbf{r}_S(t_r) \tag{12}$$

with $S \in \{\text{L}, \text{R}\}$ while $\bar{\mathbf{B}}_{\text{L}}$ and $\bar{\mathbf{B}}_{\text{R}}$ correspond to the last and first $N+1$ rows of $\bar{\mathbf{B}}$, respectively. $\bar{\mathbf{p}}_{\text{L}}(t_r)$ and $\bar{\mathbf{p}}_{\text{R}}(t_r)$ represent the synchrophasors and their derivatives in the left and right subwindows, respectively.

Let us also introduce the weighting vectors $\mathbf{w}_{\text{L}}$ and $\mathbf{w}_{\text{R}}$ (and the corresponding diagonal matrices $\mathbf{W}_S = \text{diag}(\mathbf{w}_S)$) made of the last and first $N+1$ components of $\mathbf{w}$. Under the usual assumptions, the estimates $\hat{\bar{\mathbf{p}}}_{\text{L}}(t_r)$ and $\hat{\bar{\mathbf{p}}}_{\text{R}}(t_r)$ of the synchrophasors and their derivatives in t_r computed, respectively, from the left and right portions of the samples (which will be often referred to as the left and right estimates) are obtained with the WLS approach, hence minimizing the Euclidean norm of $\mathbf{r}_{w,S}(t_r) = \mathbf{W}_S \mathbf{r}_S(t_r)$. Their general expression is given by

$$\hat{\bar{\mathbf{p}}}_S(t_r) = \bar{\mathbf{B}}^{\dagger}_{w,S} \mathbf{x}_{w,S}(t_r) = \bar{\mathbf{H}}_{w,S} \mathbf{x}_S(t_r) \tag{13}$$

with $\bar{\mathbf{B}}_{w,S} = \mathbf{W}_S \bar{\mathbf{B}}_S$ and $\mathbf{x}_{w,S}(t_r) = \mathbf{W}_S \mathbf{x}_S(t_r)$.

From (13), two different banks of filters, represented by the rows of $\bar{\mathbf{H}}_{w,\text{L}}$ and $\bar{\mathbf{H}}_{w,\text{R}}$, for left and right estimations, respectively, are found. It is interesting to note that $\bar{\mathbf{H}}_{w,\text{L}}$ corresponds to causal filters, while $\bar{\mathbf{H}}_{w,\text{R}}$ defines purely noncausal ones, with respect to t_r. Through this complementarity, it is guaranteed that one of the two sets of estimates (phasor, frequency, and ROCOF) is free from artifacts due to the step.

B. Blending Left and Right Estimates

The next problem to be faced is how to exploit the estimates computed in the left and right subwindows to achieve exemplary responsiveness in the presence of fast dynamics, without sacrificing disturbance rejection under slowly varying conditions. In [27], the proposed PMU algorithm computes the estimates obtained from three TFM models: one covering the full observation window, the second considering the left subwindow, and the third based on the right subwindow, as explained in the previous Section III-A. Proper decision rules enable returning the best estimate, according to the peculiar operating condition, by processing the norms of the left and right residuals. In the presence of slow dynamics, both the residuals are either very small or extremely similar; in this case, the method returns the results obtained from the whole set of samples, which is the most robust with respect to superimposed disturbances. Conversely, in the presence of an abrupt transition in either the left or right subwindow, the corresponding residual is considerably higher than the other; the estimate associated with the smallest residual is returned.

As from the results reported in [27], the technique has proven to be extremely effective, but such performance is attained thanks to the careful tuning of two threshold values. Such thresholds depend on several factors, including the structure of the adopted TFM model, the noise and disturbance level, and the minimum amplitude step that has to be detected. To overcome this limitation, the target of the present article is proposing a new method to blend the left and right estimates into a unique value not affected by user-selected thresholds. The basic ideas are summarized in what follows.

1) The returned estimate should rely more on $\hat{\bar{\mathbf{p}}}_{\text{L}}$ or $\hat{\bar{\mathbf{p}}}_{\text{R}}$ according to their relative quality level;
2) If the quality of $\hat{\bar{\mathbf{p}}}_{\text{L}}$ and $\hat{\bar{\mathbf{p}}}_{\text{R}}$ is virtually identical, the estimate should correspond to that obtained from a TFM model fitted on the whole set of samples;
3) The transition between left, full, and right estimates should be seamless.

To reach this target, let us select a proper TFM model and vector $\mathbf{w}$, typically generated from a window function. For a given vector of samples, the WLS estimates of the synchrophasors and their derivatives (that is $\hat{\bar{\mathbf{p}}}$) are obtained through (9), but adopting a new, dynamically adjusted vector of weights $\mathbf{w}_{\mathrm{LR}} = \mathbf{w}_\alpha \circ \mathbf{w}$, where $\circ$ denotes the Hadamard product, while

$$\mathbf{w}_\alpha = \begin{bmatrix} \alpha_{\mathrm{R}} \mathbf{1}_N \\ 1 \\ \alpha_{\mathrm{L}} \mathbf{1}_N \end{bmatrix} \tag{14}$$

having introduced $\mathbf{1}_N$ as the size N column vector of ones. The coefficients α_{L} and α_{R} appearing in (14) are

$$\begin{aligned} \alpha_{\mathrm{L}} &= \min(1-\lambda, 1) \\ \alpha_{\mathrm{R}} &= \min(1+\lambda, 1). \end{aligned} \tag{15}$$

Both α_{L} and α_{R} depend on a real-valued parameter $\lambda \in [-1, 1]$, which should reflect the relative quality of the left and right estimates. In this respect, $\lambda = -1$ means that it is worth trusting exclusively the left estimate; in fact, in this case $\alpha_{\mathrm{L}} = 1$, $\alpha_{\mathrm{R}} = 0$, hence the WLS solution obtained with the weighting vector $\mathbf{w}_{\mathrm{LR}}$ corresponds to the left estimate given by (13) with $S = \mathrm{L}$. The opposite situation should result in $\lambda = 1$: it implies $\alpha_{\mathrm{L}} = 0$, $\alpha_{\mathrm{R}} = 1$, hence $\hat{\bar{\mathbf{p}}} = \hat{\bar{\mathbf{p}}}_{\mathrm{R}}$. Finally, if $\lambda = 0$, we have $\alpha_{\mathrm{L}} = \alpha_{\mathrm{R}} = 1$, so that $\mathbf{w}_{\mathrm{LR}} = \mathbf{w}$: in that case, the usual WLS estimate computed from the whole set of samples is obtained.

Having explained the foundation of the method, it is interesting to derive the analytic expression of $\hat{\bar{\mathbf{p}}}$, thus investigating its connection to $\hat{\bar{\mathbf{p}}}_{\mathrm{L}}$ and $\hat{\bar{\mathbf{p}}}_{\mathrm{R}}$. Reminding the WLS solution (9) with the newly defined weighting vector $\mathbf{w}_{\mathrm{LR}}$, introducing $^{\mathsf{H}}$ as the conjugate transpose operator, it requires computing

$$\hat{\bar{\mathbf{p}}}(t_r) = \bar{\mathbf{H}}_{w,\mathrm{LR}} \mathbf{x}(t_r) = \left(\bar{\mathbf{B}}_w^{\mathsf{H}} \mathbf{W}_\alpha^2 \bar{\mathbf{B}}_w\right)^{-1} \bar{\mathbf{B}}_w^{\mathsf{H}} \mathbf{W}_\alpha^2 \mathbf{x}_w(t_r) \tag{16}$$

where $\mathbf{W}_\alpha = \mathrm{diag}\,(\mathbf{w}_\alpha)$, while $\bar{\mathbf{B}}_w$ and $\mathbf{x}_w(t_r)$ are still given by (8). $\bar{\mathbf{H}}_{w,\mathrm{LR}}$ represents a bank of FIR filters, whose behavior can be modified on the run by acting on the parameter λ. Let us partition $\bar{\mathbf{B}}_w$ and $\mathbf{x}_w(t_r)$ as

$$\bar{\mathbf{B}}_w = \begin{bmatrix} \bar{\mathbf{B}}_{w,\mathrm{R\text{-}C}} \\ \bar{\mathbf{b}}_{w,\mathrm{C}}^{\mathsf{T}} \\ \bar{\mathbf{B}}_{w,\mathrm{L\text{-}C}} \end{bmatrix} \qquad \mathbf{x}_w(t_r) = \begin{bmatrix} \mathbf{x}_{w,\mathrm{R\text{-}C}}(t_r) \\ x_{w,\mathrm{C}}(t_r) \\ \mathbf{x}_{w,\mathrm{L\text{-}C}}(t_r) \end{bmatrix} \tag{17}$$

$\bar{\mathbf{b}}_{w,\mathrm{C}}^{\mathsf{T}} = \bar{\mathbf{B}}_w[N+1, *]$ is the central row of $\bar{\mathbf{B}}_w$, while $\bar{\mathbf{B}}_{w,\mathrm{R\text{-}C}}$ and $\bar{\mathbf{B}}_{w,\mathrm{L\text{-}C}}$ contain its first and last N rows, respectively. Similarly, $x_{w,\mathrm{C}}(t_r)$ is the central element of $\mathbf{x}_w(t_r)$, while $\mathbf{x}_{w,\mathrm{R\text{-}C}}(t_r)$ and $\mathbf{x}_{w,\mathrm{L\text{-}C}}(t_r)$ are made of the first and last N components. Substituting (17) into (16) allows obtaining

$$\begin{aligned} \hat{\bar{\mathbf{p}}}(t_r) = &\left(\alpha_{\mathrm{L}}^2 \bar{\mathbf{G}}_{w,\mathrm{L\text{-}C}} + \bar{\mathbf{G}}_{w,\mathrm{C}} + \alpha_{\mathrm{R}}^2 \bar{\mathbf{G}}_{w,\mathrm{R\text{-}C}}\right)^{-1} \\ &\times \left(\alpha_{\mathrm{L}}^2 \bar{\mathbf{B}}_{w,\mathrm{L\text{-}C}}^{\mathsf{H}} \mathbf{x}_{w,\mathrm{L\text{-}C}} + \underline{\mathbf{b}}_{w,\mathrm{C}} x_{w,\mathrm{C}} + \alpha_{\mathrm{R}}^2 \bar{\mathbf{B}}_{w,\mathrm{R\text{-}C}}^{\mathsf{H}} \mathbf{x}_{w,\mathrm{R\text{-}C}}\right) \end{aligned} \tag{18}$$

having defined the matrices $\bar{\mathbf{G}}_{w,S\text{-}\mathrm{C}} = \bar{\mathbf{B}}_{w,S\text{-}\mathrm{C}}^{\mathsf{H}} \bar{\mathbf{B}}_{w,S\text{-}\mathrm{C}}$ and $\bar{\mathbf{G}}_{w,\mathrm{C}} = \underline{\mathbf{b}}_{w,\mathrm{C}} \bar{\mathbf{b}}_{w,\mathrm{C}}^{\mathsf{T}}$.

It is worth noting that $\bar{\mathbf{B}}_{w,\mathrm{R\text{-}C}}$ and $\bar{\mathbf{B}}_{w,\mathrm{L\text{-}C}}$ can be, respectively, obtained by removing the last row from $\bar{\mathbf{B}}_{w,\mathrm{R}}$ and the first row from $\bar{\mathbf{B}}_{w,\mathrm{L}}$, as defined in Section III-A. Manipulating (18) while using (13), we obtain

$$\begin{aligned} \hat{\bar{\mathbf{p}}}(t_r) = &\left(\alpha_{\mathrm{L}}^2 \bar{\mathbf{G}}_{w,\mathrm{L}} + \left(1 - \alpha_{\mathrm{L}}^2 - \alpha_{\mathrm{R}}^2\right) \bar{\mathbf{G}}_{w,\mathrm{C}} + \alpha_{\mathrm{R}}^2 \bar{\mathbf{G}}_{w,\mathrm{R}}\right)^{-1} \\ &\times \left(\alpha_{\mathrm{L}}^2 \bar{\mathbf{G}}_{w,\mathrm{L}} \hat{\bar{\mathbf{p}}}_{\mathrm{L}} + \left(1 - \alpha_{\mathrm{L}}^2 - \alpha_{\mathrm{R}}^2\right) \underline{\mathbf{b}}_{w,\mathrm{C}} x_{w,\mathrm{C}} + \alpha_{\mathrm{R}}^2 \bar{\mathbf{G}}_{w,\mathrm{R}} \hat{\bar{\mathbf{p}}}_{\mathrm{R}}\right) \end{aligned} \tag{19}$$

with $\bar{\mathbf{G}}_{w,S} = \bar{\mathbf{B}}_{w,S}^{\mathsf{H}} \bar{\mathbf{B}}_{w,S}$. According to the previous equation, $\hat{\bar{\mathbf{p}}}(t_r)$ can be computed as a linear combination of the estimates obtained from the left and right subwindows. A correction related with the central sample $x_{w,\mathrm{C}}$ is also present, since it corresponds to the overlap between $\mathbf{x}_{w,\mathrm{L}}(t_r)$ and $\mathbf{x}_{w,\mathrm{R}}(t_r)$ that have been processed to obtain $\hat{\bar{\mathbf{p}}}_{\mathrm{L}}$ and $\hat{\bar{\mathbf{p}}}_{\mathrm{R}}$.

The last aspect to be discussed is the definition of the coefficient λ, which should affect the balance between the left and right estimates on the basis of their relative trustworthiness. In particular, it should dramatically reduce the weight of a subwindow as long as it is likely to include an abrupt transient. Such a fast transition is clearly well outside the TFM model subspace: this results in a notable increase in the Euclidean norm of the corresponding weighted residual, which is the cost function minimized by the WLS problem. $\|\mathbf{r}_{w,\mathrm{L}}\|$ and $\|\mathbf{r}_{w,\mathrm{R}}\|$ could thus be considered as inversely proportional to the quality level of the corresponding estimates. It is therefore reasonable to choose α_{L} and α_{R}, namely, the scaling of the weights of the samples in the left and right subwindows, so that they are inversely proportional to $\|\mathbf{r}_{w,\mathrm{L}}\|$ and $\|\mathbf{r}_{w,\mathrm{R}}\|$. According to this choice, using (15), we have

$$\lambda = \begin{cases} -1 + \dfrac{\|\mathbf{r}_{w,\mathrm{L}}\|}{\|\mathbf{r}_{w,\mathrm{R}}\|} & \text{if } \|\mathbf{r}_{w,\mathrm{R}}\| \geq \|\mathbf{r}_{w,\mathrm{L}}\| \\ 1 - \dfrac{\|\mathbf{r}_{w,\mathrm{R}}\|}{\|\mathbf{r}_{w,\mathrm{L}}\|} & \text{if } \|\mathbf{r}_{w,\mathrm{R}}\| < \|\mathbf{r}_{w,\mathrm{L}}\|. \end{cases} \tag{20}$$

Summarizing, once the TFM model (thus matrix $\bar{\mathbf{B}}$) and the weighting vector $\mathbf{w}$ are defined, the steps required to obtain synchrophasor, frequency, and ROCOF estimates from $\mathbf{x}(t_r)$ by adopting the proposed method, called $\mathrm{TFM}_{\mathrm{WRLR}}$ (TFM with weighted reconstruction from the left and right estimates), are the following.

1) Apply $\mathbf{w}$ to $\mathbf{x}(t_r)$, obtain $\hat{\bar{\mathbf{p}}}_{\mathrm{L}}(t_r)$, $\hat{\bar{\mathbf{p}}}_{\mathrm{R}}(t_r)$ with (13).
2) Evaluate the norms of the left and right residuals, which enable obtaining λ (i.e., also α_{L} and α_{R}) and thus computing $\hat{\bar{\mathbf{p}}}(t_r)$ from (19).
3) Synchrophasor, frequency, and ROCOF estimates in the measurement instant t_r are finally derived from the first three components of $\hat{\bar{\mathbf{p}}}(t_r)$ (see [25]).

These stages are also schematically summarized by means of the flowchart shown in Fig. 1. For the sake of clarity, the recombined estimate $\hat{\bar{\mathbf{p}}}$ is shown in yellow, while quantities referring to the left or right subwindow are represented in blue and green, respectively. From now on, these colors will be used.

One important novelty of the proposed method is that it does no longer rely on thresholds to choose between the left and right estimates. Now a merging procedure based on weighting is adopted, without a dedicated step detection stage. A minimum residual threshold might be used to address clean

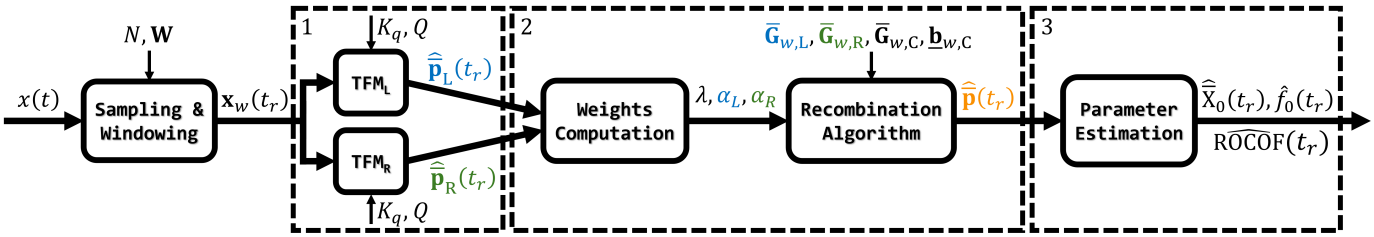

Fig. 1. Flowchart of the proposed TFM_{WRLR} algorithm.

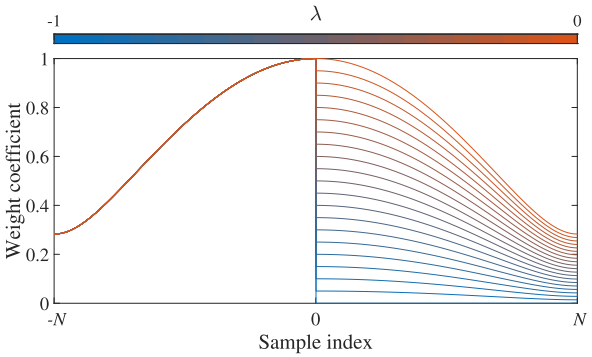

Fig. 2. Weight coefficients (components of $\mathbf{w}_{\text{LR}}$) parameterized by $-1 \leq \lambda \leq 0$.

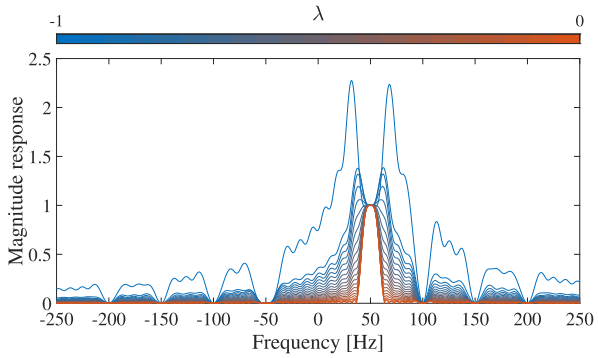

Fig. 3. Magnitude response of the family of filters that enable estimating $\hat{X}_0$ parameterized by $-1 \leq \lambda \leq 0$.

signals as in [27] (if $\|\mathbf{r}_{w,\text{R}}\|$ and $\|\mathbf{r}_{w,\text{L}}\|$ are very small, λ is ill-defined) but this becomes irrelevant as soon as wideband noise, even very low, is present.

IV. Test Results

The proposed method TFM_{WRLR} has been implemented in MATLAB environment considering $f_0 = 50\,\text{Hz}$, adopting $T_w = 180\,\text{ms} + T_s$. This corresponds to a window of about nine nominal cycles (and thus left and right half windows of about 4.5 cycles), while keeping an odd number of samples according to the assumption of Sections II and III. The target reporting rate (RR) is 50 fps and this value is used for setting the limits in terms of PMU pass-bandwidth and standard requirements. A third-degree expansion has been adopted for the fundamental term, hence $K_0 = 3$. Like in [27], harmonics up to the fourth order have been included in the TFM model using first-degree expansions (i.e., $K_q = 1$, $q \in \{1, 2, 3\}$), and thus higher order harmonics are not part of it regardless their possible presence in the signals. The reason for this choice is that, thanks to the frequency separation and the decaying sidelobes of the filters, they produce weak interference with the fundamental estimates. Different windows can be chosen, but an optimization of window weights is beyond the scope of this article. In the following tests, vector $\mathbf{w}$ is generated as the square root of the Hamming window.

Fig. 2 shows, for $-1 \leq \lambda \leq 0$, the resulting values of the weight coefficients applied to the samples, namely, the elements of vector $\mathbf{w}_{\text{LR}}$. Opposite (positive) values of λ would have resulted in mirrored weights with respect to sample index $n = 0$.

Having defined the TFM model, for a given value of λ it is possible to compute the frequency responses of the FIR filters defined by the rows of matrix $\bar{\mathbf{H}}_{w,\text{LR}}$. In this respect, Fig. 3 shows the magnitude response of the filter that allows extracting the synchrophasor for $-1 \leq \lambda \leq 0$ (the shape is not affected by the sign of λ). Amplitude is unitary at the reference fundamental frequency, while multiple zeros are present at the harmonic frequencies included into the model. It is worth highlighting that as $|\lambda|$ increases, a significant rise of the sidelobes occurs. This results in higher sensitivity to wideband disturbances, hence it has key importance that λ is close to zero, except in the presence of abrupt transients.

The reference frequency of the TFM model is updated according to the previous frequency measurement using a coarse 1 Hz grid to address large frequency deviations as in [16], [32]. This means that when frequency undergoes strong variations with respect to its rated value, like in off-nominal frequency and ramp tests, a few TFM model transitions can occur. Being them based on precomputed filters, they do not affect computational burden.

To reduce the slight fluctuations that can occur in noisy conditions, the value of $|\lambda|$ can be rounded to 1, e.g., when $|\lambda| > 0.86$ (i.e., when a 2 % ratio among left and right, or vice versa, residual energies is obtained) at run time.

It is important to highlight that the specific method configuration is mainly considered here as an example of settings that allow the solution found using the TFM model on the full window to be compliant with class M requirements of the PMU Std. The parameters (expansion degrees, window length, included components, weighing, etc.) arise from a tradeoff between different needs (harmonics or interharmonic rejection, dynamics tracking, etc.), and thus different settings allow compliance.

Moreover, the proposed approach can also be combined with other techniques, in particular those based on an adaptive TFM model for canceling narrowband interferers [24], [31]: in this

TABLE I
WORST CASE ERRORS FOR M-CLASS STEADY-STATE AND DYNAMIC COMPLIANCE TESTS (TFM AND TFM_{WRLR} ALGORITHMS)

Test	AE [%]	PE [crad]	TVE [%]	Std [%]	FE [mHz]	Std [mHz]	RFE [Hz/s]	Std [Hz/s]
nominal	$1.0{\cdot}10^{-3}$	$1.1{\cdot}10^{-3}$	$1.4{\cdot}10^{-3}$	1	0.07	5	$1.6{\cdot}10^{-3}$	0.1
signal freq. ($f_0 \pm 5$ Hz)	$1.9{\cdot}10^{-3}$	$1.7{\cdot}10^{-3}$	$1.9{\cdot}10^{-3}$	1	0.11	5	$2.9{\cdot}10^{-3}$	0.1
harm. dist. (THD = 10 %)*	$2.6{\cdot}10^{-3}$	$2.7{\cdot}10^{-3}$	$2.7{\cdot}10^{-3}$	1	1.89	5	$7.9{\cdot}10^{-3}$	-
out-of-band (50.0 Hz, TIHD = 10 %)	$5.9{\cdot}10^{-2}$	$6.2{\cdot}10^{-2}$	$6.2{\cdot}10^{-2}$	1.3	9.27	10	0.32	-
out-of-band (52.5 Hz, TIHD = 10 %)	$7.3{\cdot}10^{-2}$	$7.3{\cdot}10^{-2}$	$7.4{\cdot}10^{-2}$	1.3	8.31	10	0.38	-
out-of-band (47.5 Hz, TIHD = 10 %)	$7.4{\cdot}10^{-2}$	$7.3{\cdot}10^{-2}$	$7.4{\cdot}10^{-2}$	1.3	8.95	10	0.34	-
phase mod. ($f_m \leq 5$ Hz)	0.23	0.46	0.47	3	23.1	300	4.40	14
ampl. mod. ($f_m \leq 5$ Hz)	0.51	$9.6{\cdot}10^{-3}$	0.51	3	2.34	300	$4.7{\cdot}10^{-2}$	14
freq. ramp (ROCOF = +1 Hz/s)	$1.9{\cdot}10^{-3}$	$3.0{\cdot}10^{-3}$	$3.0{\cdot}10^{-3}$	1	0.09	10	$2.5{\cdot}10^{-2}$	0.2
freq. ramp (ROCOF = −1 Hz/s)	$2.0{\cdot}10^{-3}$	$3.3{\cdot}10^{-3}$	$3.3{\cdot}10^{-3}$	1	0.10	10	$2.4{\cdot}10^{-2}$	0.2

*The worst-case performance is obtained in the presence of the 5th order harmonic.

case, M-class compliance can be achieved with lower latency. However, these solutions have not been considered here for the sake of a more concise explanation. In this respect, there is no presumption to reach "optimal" performance, but rather to clearly illustrate the potentialities of the proposal based on merging left and right TF expansions. From a different point of view, it is very significant to implement the method starting from a rather long TFM model, typically implying slow responsiveness.

A. Steady-State and Dynamic Tests

To validate the proposed method, its performance has been characterized over the entire test set for M-class compliance prescribed by the PMU Std. The results are compared with those achieved by the conventional TFM approach. If not otherwise specified, the test waveforms have 10 s overall duration and estimates have been computed sample by sample. This measurement rate has been used only for testing purposes since, for each condition, this yields a statistically relevant sample of phasor, frequency and ROCOF measurements. The results are thus more representative and define a conservative scenario in terms of errors. Indeed, this also allows for considering the dependence on different combinations of signal parameters (i.e., frequency and initial phase). Nevertheless, it is important to note that the algorithm is intended to operate with an RR of 50 fps, and this value is adopted when looking at the PMU Std limits. For step tests, in particular, the sample-by-sample approach allows a better excitation of the algorithm and a finer description of the step response with respect to the usual PMU testing procedure.

For each test, performance is assessed in terms of amplitude error (AE), phase error (PE), total vector error (TVE), frequency error (FE), and ROCOF error (RFE). In this regard, Table I reports the worst case values in all the static and dynamic compliance tests and, when applicable, it compares them against the corresponding PMU Std requirements. To account for the measurement noise introduced by the acquisition process, if not explicitly mentioned, error indexes are obtained in the presence of additive white uniform noise with 80-dB signal-to-noise ratio (SNR).

Considering all the test conditions, the proposed method proves to be fully M-class compliant. In the static tests, it provides virtually the same results as TFM, which are thus not reported in Table I. This proves the validity and robustness of the method. It is important to highlight that in such conditions, the left and right estimates are combined with similar weights, and thus it is like computing the expansion on the entire window. Very low errors are achieved both under off-nominal frequency conditions (thanks to the adaptive reference frequency of the TFM model) and in the harmonic distortion test. In that case, the highest error occurs in the presence of the 5th-order harmonic, namely, the lowest that has not been embedded in the signal model. Worst performance is obtained in the *out-of-band* test. This result derives directly from the selected structure for the TFM model, which only includes the first four harmonics, and thus, it does not account for possible interharmonics. The uncompensated effect of the interharmonics causes a nonnegligible error, particularly in terms of FE and RFE, but it still remains within class M requirements.

Considering dynamic conditions, the TFM_{WRLR} method still reconstructs almost exactly the TFM estimate (i.e., λ is always close to zero), thus achieving the same errors (not reported in Table I). All the maximum errors are largely within the corresponding requirements, thanks to the inherently dynamic model of the fundamental component embedded in the TFM expansion. This is particularly effective for modulated signals, while during *frequency ramp* tests (from 45 to 55 Hz or vice versa) the frequency tuning also comes into play for keeping the errors low. As previously mentioned, the change in the TFM reference frequency does not impact the computational burden.

The next step is analyzing the impact on the proposed algorithm of different noise levels and sampling rates under nominal conditions. Let us suppose that samples are affected by additive, independent noise having variance $\sigma^2 \ll |\bar{X}_0|^2$. For given values of the parameters λ and length T_w, it is possible to prove that for M large enough, the estimation errors induced by superimposed noise have Gaussian distributions, whose variances are proportional to σ^2 and inversely proportional to M. Moreover, it is interesting to stress that $\|\mathbf{r}_{w,\text{L}}\|^2$ and $\|\mathbf{r}_{w,\text{R}}\|^2$ are purely due to noise: therefore, reminding (20), λ approaches zero. For this very reason, noise rejection of the TFM_{WRLR} algorithm is expected to be virtually identical to that of the conventional TFM method.

These considerations are fully confirmed by the simulation results. Table II reports the maximum (Max) and root mean square (rms) values of TVE, FE, and RFE obtained with TFM

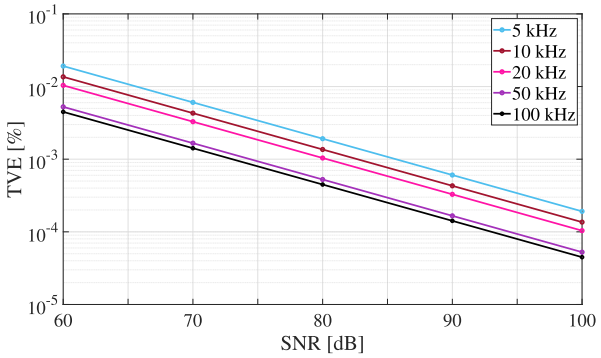

Fig. 4. Maximum TVE for TFM and TFM_{WRLR} algorithms with different SNRs and sampling frequencies.

TABLE II

MAXIMUM AND RMS ERRORS FOR DIFFERENT SNRS IN NOMINAL CONDITIONS (TFM AND TFM_{WRLR} ALGORITHMS)

SNR [dB]	TVE [%] Max / rms	FE [mHz] Max / rms	RFE [Hz/s] Max / rms
60	$1.4 / 0.6 \cdot 10^{-2}$	$7.4 / 2.5 \cdot 10^{-1}$	$1.7 / 0.6 \cdot 10^{-3}$
70	$4.3 / 1.9 \cdot 10^{-3}$	$2.3 / 0.8 \cdot 10^{-1}$	$5.4 / 1.9 \cdot 10^{-3}$
80	$1.4 / 0.6 \cdot 10^{-3}$	$7.4 / 2.5 \cdot 10^{-2}$	$1.7 / 0.6 \cdot 10^{-3}$
90	$4.3 / 1.9 \cdot 10^{-4}$	$2.3 / 0.8 \cdot 10^{-2}$	$5.4 / 1.9 \cdot 10^{-4}$
100	$1.4 / 0.6 \cdot 10^{-4}$	$7.4 / 2.5 \cdot 10^{-3}$	$1.7 / 0.6 \cdot 10^{-4}$

and TFM_{WRLR} methods (values are identical), which exhibit a linear increase with noise variance. Furthermore, Fig. 4 shows the maximum TVE achieved by both TFM_{WRLR} and TFM as a function of the SNR for different sampling frequencies. As expected, the TVE has a linear trend in the log–log plot, being it proportional to the noise standard deviation. Moreover, the graph shows that as the sampling rate increases, the impact of SNR on TVE reduces proportionally to $(T_s)^{1/2}$.

B. Amplitude and Phase Step Tests

As previously discussed, the main advantage of the proposed method consists in its capability of minimizing the estimation errors resulting from filter dynamics triggered by abrupt transients. To prove that, we perform the *step change* tests of the PMU Std both without and with additive noise. The first case enables verifying the validity of the mathematical treatise under ideal conditions. The second case assesses the robustness of the proposed method in the presence of wideband disturbances, other than evaluating possible degradation of the equivalent noise bandwidth introduced by the merging process. Tests have been carried out with both positive and negative steps; since the obtained results and trends are virtually identical, the analysis will be limited to positive steps.

First, the 10 % amplitude step under noiseless conditions is considered. In this case, the TVE of the conventional TFM implementation reaches 5 % with the RT exceeding 42.51 ms. Conversely, TVE values are negligible if the TFM_{WRLR} approach is adopted, resulting in zero RT since the 1 % steady-state limit is never reached. The parameter λ initially starts from small values, and thus, estimation is performed on the full window such as in the classic TFM approach. However, its value rapidly decreases to -1 as long as the step enters in the right half window (recombination discards automatically this part), jumps to 1 when the step moves to the left part (measurements fully rely on the right half window) and then it decreases again to zero when the step leaves also the left side of the window. Similar conclusions can be drawn when looking at the results in terms of FE and RFE, with the TFM algorithm reaching peaks that exceed 20 mHz and 0.55 Hz/s, respectively, while the corresponding RTs are about 95 and 138 ms. Conversely, the TFM_{WRLR} technique ensures negligible FE and RFE, therefore zero RTs also for frequency and ROCOF measurements.

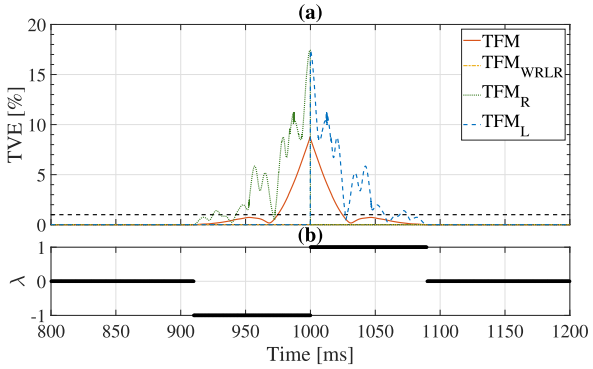

Fig. 5. Phase step test in noiseless conditions. (a) Time evolution of TVE for TFM (solid red), TFM_{WRLR} (dash-dotted yellow), TFM_{R} (dash-dotted green), and TFM_{L} (dash-dotted blue) algorithms. (b) Time evolution of λ.

The TFM_{WRLR} method reaches exemplary performance also in the presence of the 10° phase step, with negligible TVE, FE, and RFE values, corresponding to zero RTs. In this respect, the upper subplot of Fig. 5 reports the time evolution of the TVE for both the considered algorithms and for the estimates purely obtained from the left and right subwindows (TFM_{L} and TFM_{R}), respectively, with the transient occurring in $t = 1$ s. The maximum TVE is well above 8 % for the TFM technique, with an RT of nearly 50 ms; it is worth noting that the plot shows local maxima that are not negligible with respect to the steady-state limit, located about 45 ms before and after the step instant. The TVEs of the TFM_{R} and TFM_{L} allow a better understanding of the benefits obtained recombining by means of appropriate weights the results of the left and right TF expansions. The perfectly mirrored TFM_{R} and TFM_{L} curves exhibit almost zero TVE in the time intervals after and before the step instant, respectively, a maximum TVE of about 18 % and some smaller local maxima in the mirrored intervals. Thus, they have almost ideal behavior when their contribution to the merged estimate is dominant and vice versa.

In addition, the lower subplot of Fig. 5 shows the time evolution of λ, which blends the results of the left and right expansions in the TFM_{WRLR} method. The behavior is similar to that described for the amplitude step, with λ close to 0 as the step is not within the processed time interval. Conversely, when the step occurrence enters the right side of the window, λ is nearly -1, meaning that the results of the TFM_{WRLR} are practically the same of the left expansion. Conversely, when the occurrence of the step enters the left side of the window, λ is close to 1, and thus, the results of TFM_{WRLR} are practically the same as those of the right expansion. In this way, it is possible to keep the TVE way below the steady-state limit. Conversely, the classic TFM results in extremely high peaks

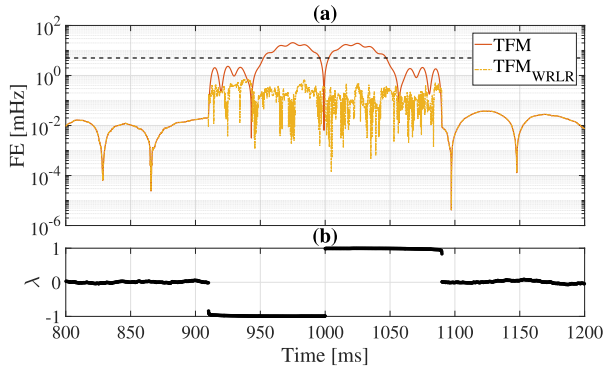

Fig. 6. Amplitude step test with 80-dB SNR. (a) Time evolution of FE (semilog scale) for TFM (solid red) and TFM_{WRLR} (dash-dotted yellow) algorithms. (b) Time evolution of λ.

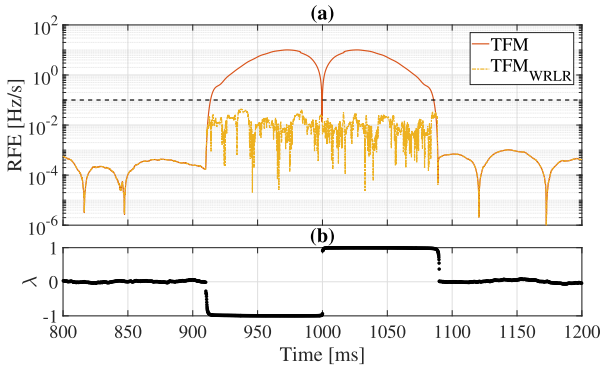

Fig. 7. Phase step test with 80-dB SNR. (a) Time evolution of RFE (semilog scale) for TFM (solid red) and TFM_{WRLR} (dash-dotted yellow) algorithms. (b) Time evolution of λ.

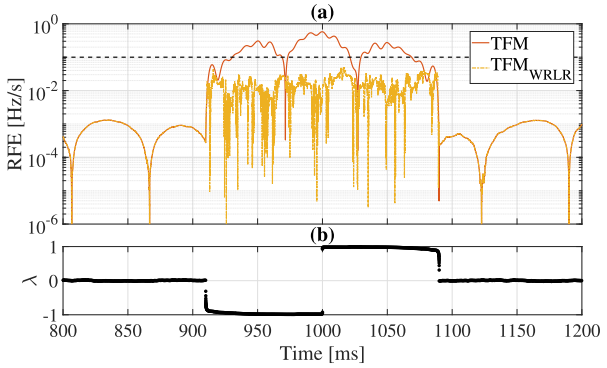

Fig. 8. Amplitude step test with 72-dB SNR, $f_s = 50$ kHz. (a) Time evolution of RFE (semilog scale) for TFM (solid red) and TFM_{WRLR} (dash-dotted yellow) algorithms. (b) Time evolution of λ.

in term of FE and RFE values, above 600 mHz and 10 Hz/s, with RTs longer than 170 ms.

As mentioned above, the previously described step tests have been repeated with 80 dB SNR. In this respect, the TFM method always relies on the full vector of the samples: therefore, thanks to the averaging effect, estimates shall be rather immune to noise. On the contrary, TFM_{WRLR} may discard N samples out of $2N + 1$: this unavoidably increases noise infiltration. In turn, it may jeopardize frequency and ROCOF estimates, notably the most affected by noise since the estimation algorithm is asked to compute derivatives. The results confirm that, as expected, the performance achieved with the TFM method is barely affected by noise, in terms of both maximum errors and RTs. However, also the behavior of the TFM_{WRLR} method in the presence of step variations has proven to be robust with respect to wideband noise. In all the cases, TVE, FE, and RFE values remain very small when compared with the corresponding steady-state limits prescribed by the PMU Std. Therefore, zero RT is also attained under these more demanding (and realistic) operating conditions.

As an example, Fig. 6(a) shows the trend of the FEs of both the methods, with an amplitude step occurring in $t = 1$ s. It is possible to see that as the FE of the TFM method starts to rise, we have a nonnegligible increase in that achieved by the TFM_{WRLR} technique. In this case, the relative weights of the left and right subwindows are becoming very different, hence the dynamically adjusted FIR filters have worse equivalent noise bandwidth under these conditions. Nevertheless, FE remains below 0.7 mHz. With respect to the noiseless case in Fig. 5, it is worth noting how the lambda evolution (ee Fig. 6(b)) presents, when the step is not inside the observation window, a noisy trend (spanning from 0.08 to -0.07). In the presence of step changes, λ shows a slightly less abrupt transition when compared with the noiseless case. The reason is that noise produces virtually identical additive contributions to $\|\mathbf{r}_{w,\text{R}}\|^2$ and $\|\mathbf{r}_{w,\text{L}}\|^2$ (proportional to its variance) that reduce $|\lambda|$. Nevertheless, the proposed method is still capable of precisely detecting the step occurrence (within few samples) and selecting the most suitable portion of the signal window.

Considering the phase step at 80 dB SNR, Fig. 7(a) reports the time evolution of the RFEs obtained by the considered algorithms. The same behavior previously observed in Fig. 6(a) here becomes more notable. ROCOF computation is based on a second-order differentiation, thus being even more sensitive to wideband noise. The increase in RFE that occurs when the TFM_{WRLR} method starts trusting only one of the subwindows is evident, but its peak value remains an order of magnitude below the steady-state limit, whereas TFM strongly suffers step infiltration. When compared with Fig. 6(b), in the presence of step changes, λ (see Fig. 7(b)) exhibits a smoother trend, but this does not affect the effectiveness of TFM_{WRLR}.

The robustness of the proposed algorithm has been assessed through phase and amplitude steps with higher noise level. In this respect, 72-dB SNR with $f_s = 50$ kHz has been considered, thus mimicking a 12-bit acquisition stage like, e.g., in [33]. The results show that the RTs to amplitude and phase step are virtually identical to those obtained in noiseless conditions; in particular, the TFM_{WRLR} method still features zero RT. As an example, the higher subplot of Fig. 8 reports the RFE achieved by TFM and TFM_{WRLR} during an amplitude step. The lower subplot of Fig. 8 shows the evolution of λ, which is less sharp with respect to the previous amplitude step case of Fig. 6, but this does not impact on the overall performance.

The step tests with 80 dB SNR have been repeated when the transition between the two steady-states has finite slope. In particular, a fast but not nil transient duration is considered,

TABLE III
RT OF TVE, FE, AND RFE FOR TFM AND TFM_{WRLR} IN LINEAR AMPLITUDE TRANSITIONS OF DIFFERENT DURATIONS

Step Duration Δt [ms]	RT_{TVE} [ms]		RT_{FE} [ms]		RT_{RFE} [ms]	
	TFM	TFM_{WRLR}	TFM	TFM_{WRLR}	TFM	TFM_{WRLR}
0	42.5	0	94.6	0	138.4	0
4	42.0	0.2	63.7	3.3	101.4	3.6
8	41.9	0	51.8	7.1	53.2	7.5

where the quantity of interest (magnitude or phase angle) linearly varies between pre- and post-transient values in Δt milliseconds. Table III reports the RT obtained in repeated tests with different Δt values. TVE RT is almost constant for both TFM and TFM_{WRLR}, corresponding to the value already found with instantaneous step ($\Delta t = 0$ ms in the table). Indeed, TFM_{WRLR} RT slightly increases since few measurements may exceed the steady-state threshold limit ($\Delta t = 4$ ms). This is due to the reduced leverage of balancing in the middle of the window, coupled with the decreased sensitivity of the weights in the presence of slower transients. Anyway, there is also the compensating effect that a TFM model better represents a less steep transition and this justifies the zero RT for $\Delta t = 8$ ms. As for FE and RFE, the behavior of the two methods is opposite: while TFM reduces the RT when Δt increases (the TFM model is closer to the signal dynamics), TFM_{WRLR} starts showing a less prompt reaction. Once again, the steady-state error thresholds can be exceeded near the transition, and this effect is magnified by a longer duration. Obviously, the behaviors of TFM and TFM_{WRLR} approaches tend to converge for a long transient duration since, in the presence of slow variations, their measurements are the same. However, as indicated by Table III results, with $\Delta t = 8$ ms the RTs of TFM_{WRLR} are still more than seven times smaller than those achieved by TFM for both FE and RFE.

As a final comment, it is worth mentioning that RT value is strongly linked to the chosen threshold level, but, as it is patent from Figs. 5–8, the overall quality of the measurements provided by TFM_{WRLR}, when compared with a filtering algorithm like TFM, can be even better than what emerges from the mere indexes chosen by the PMU Std and this corresponds to the aim of the proposal, i.e., guaranteeing many more valid and accurate measurements notwithstanding transient conditions.

C. Analysis of Computational Burden

When dealing with the conventional TFFs, the computational load corresponds mainly (excluding frequency and ROCOF computation) to the application of the filter bank needed to estimate the synchrophasor derivatives. The load is thus $\mathcal{O}(M)$, since, considering the filters as precomputed, it is due to the application of 3 complex filters to M samples ($3M$ pairs of multiplications because samples are real-valued) to find the synchrophasor and its first two derivatives. The TFM model defines the TFFs including different components in the model (4 in the above tests), and thus, the computational cost is the same as the classic TFF.

In the proposed method instead, the window is split into two $N + 1 = (M + 1)/2$ sample segments, with one sample overlap. Thus, applying the left and right filters has almost the same cost as the usual TFFs: $3 \cdot ((M + 1)/2) \cdot 2 = 3M + 3$ pairs of multiplications, i.e., only three additional pairs, regardless the value of M. The computation cost also includes that due to (19), which is the estimates blending equation, namely, weights computation and recombination. The weights depend on λ, and thus, the cost is $\mathcal{O}(N)$, because it is related to the energy computation of the left and right residuals (see (14) and (20)). Considering the main steps, there is a matrix computation, a matrix inversion, a vector computation, and a final matrix–vector multiplication.

The matrix inversion is applied to an $N_p \times N_p$ matrix (where $N_p = \sum_{q=0}^{Q}(2K_q + 2)$ is the number of parameters in the TFM model, i.e., in $\bar{\mathbf{p}}$). In the considered implementation, the matrix is 20×20, and therefore, the inversion computational complexity is $\mathcal{O}(1)$ since it does not depend on M but only on the number Q of components in the model and their degrees K_q. This is an advantage since the matrix inversion, which could otherwise become burdensome, has indeed a limited impact if the TFM does not include many components. The matrix to be inverted is the weighted sum of the three precomputed matrices $\bar{\mathbf{G}}_{w,S}$ with $S \in \{\text{L}, \text{C}, \text{R}\}$, and thus, cost is $\mathcal{O}(1)$. It is indeed interesting to note that only some rows of the inverse matrix need to be obtained, since just three estimates are necessary to compute phasor, frequency, and ROCOF of the fundamental component. Finally, vector $\alpha_{\text{L}}^2 \bar{\mathbf{G}}_{w,\text{L}} \hat{\bar{\mathbf{p}}}_{\text{L}} + (1 - \alpha_{\text{L}}^2 - \alpha_{\text{R}}^2) \mathbf{b}_{w,\text{C}} x_{w,\text{C}} + \alpha_{\text{R}}^2 \bar{\mathbf{G}}_{w,\text{R}} \hat{\bar{\mathbf{p}}}_{\text{R}}$ in (19) requires again $\mathcal{O}(1)$, since it is the sum of three matrix–vector multiplications depending only on N_p and not on M. Without considering any optimization, the number of complex multiplications in this step is $2N_p(2N_p + 4) + 1$. Then $3 \cdot N_p$ complex multiplications are required for the final matrix–vector multiplication (limiting the calculation of $\bar{\mathbf{p}}$ to the parameters of interest).

It is important to highlight that no optimization relying on the symmetry of the matrices and the presence of conjugate numbers is considered for the sake of brevity and to focus only on the essential concepts. However, it is worth mentioning that by trading computation for memory, it is also possible to speed up the processing by precomputing and storing the intermediate matrices corresponding to discretized values of λ, thus avoiding any matrix inversion. From the above considerations, it is clear that the proposed method has a computational load comparable with that of TFFs and TFM.

Furthermore, to prove the feasibility of the method, the execution times of the TFM and the TFM_{WRLR} algorithms have been measured, using MATLAB environment (version R2022a) in a computer with Intel-Core i7-11370H at 3.30 GHz and 16-GB RAM. Considering 50 000 measurements, average processing times of 67.7 and 119.4 µs have been obtained, respectively, hence guaranteeing every standard RR. It is important to also highlight that in this case the symmetry of the matrices and the presence of conjugate numbers have not been exploited to reduce the computational complexity. For this reason, the previous results are only illustrative since they can be significantly improved by simplifying the algorithms operations.

D. Comparison Between RTs Achieved by State-of-Art PMU Algorithms

To better quantify the advantage of the proposed approach, we carried out a comparison between the RTs achieved by several M-class PMU algorithms published in the scientific literature, and by the reference M-class method proposed by [7] (denoted as **IEEE 60255-118-1:2018 M** method in the following description). All of them are configured for 50 or 60 fps RR and are also chosen as representative of different classes of algorithms; some reach simultaneous P- and M-class compliance, thanks to different expedients aimed at reducing latency. They will be briefly introduced in the following[1].

1) **IREQ FIR-M Noncausal**: In [34], noncausal and causal versions of a bandpass FIR filter (a Taylor window is used in the tests) with center frequency tuning are proposed. The noncausal algorithm (obtained through timestamp compensation) is designed to be M-class compliant for synchrophasor estimation.
2) **M-MW-FIR**: The algorithm presented in [35] is based on the interpolation of the components extracted with two bandpass FIR filters designed starting from the Morlet wavelet and centered to rated frequency.
3) **PMU Algorithm P+M**: The algorithm in [16], as already mentioned in Section I, includes two TFFs (with different degrees and lengths) and a detector to switch between them to have simultaneous P- and M-class compliance (except for RFE out-of-band limit of [36], however removed in 2014 amendment and in PMU Std [7]).
4) **i-IpDFT P+M**: This method, discussed in [8], is based on an enhanced three-point interpolated DFT that compensates the long-range leakage due to the negative frequency image. Location and removal of possible out-of-band components allow complying with both P- and M-class requirements.
5) **HT-IpDFT P+M**: This method, proposed in [19], similar to that in [8], is based on a three-point interpolated DFT and iterative removal of possible components below 150 Hz, but it processes the signal after HT application, using an event detector to switch between two HT filter outputs with different performance.
6) **FiIpDFT P+M**: The technique described in [33] can be considered as an extension of the previous i-IpDFT method [8]. It performs the measurements through three-point interpolated DFT, combined with an iterative estimation and cancellation of the interference due to out-of-band components. It achieves simultaneous P- and M-class compliance.
7) **eIpD2FT M**: The algorithm presented in [37] achieves M-class compliance with a two-cycle observation interval through preliminary detection of interferers via ESPRIT, which are suppressed by including them into a proper dynamic model of the signal.
8) **Space Vector M**: This M-class method, proposed in [38], is based on the space vector (SV) transformation of the three-phase signal adopting a reference frame that rotates at the nominal frequency. Positive sequence synchrophasor, frequency, and ROCOF estimates are obtained by filtering the magnitude and phase of the SV signal.

[1]The adopted names are only indicative and are either those used in the referenced paper or defined for presentation purposes.

TABLE IV
AMPLITUDE AND PHASE STEP RTS OF THE TVE FOR DIFFERENT STATE-OF-ART ALGORITHMS

Algorithm	RR [fps]	RT_{TVE} [ms] Amp. Step	RT_{TVE} [ms] Ph. Step
IEEE 60255-118-1:2018 M [7]	60	-*	66.0
IREQ FIR-M Non-Causal [34]	60	30.6	37.5
M-MW-FIR [35]	50	61.6	76.9
PMU Algorithm P+M [16]	50	18.0	22.0
i-IpDFT P+M [8]	50	28.0	32.0
HT-IpDFT P+M [19]	50	22.9	26.4
FiIpDFT P+M [33]	50	28.1	34.1
eIpD2FT M [37]	50	14.0	24.0
Space Vector M [38]	50	37.5	42.5
Conventional TFM M	50	42.5	50.1
Proposed TFM_{WRLR} M	50	0	0

* The standard reports only the value for the Phase Step Change test.

The results of the comparison in terms of TVE RTs are reported in Table IV. It is important to underline that there is no pretense of completeness, since a comprehensive comparison is out of the scope for this research paper. Nevertheless, the reported results can help better frame the potentialities of the proposed idea. Indeed, Table IV demonstrates the lack of algorithms that allow zero RTs for TVE, which is exactly the aim of the proposed method. Similar considerations arise when looking at FE and RFE RTs (not reported here), but it is worth noting that the SV M [38] algorithm achieves zero RT for these quantities in the amplitude step test.

V. CONCLUSION

This article has introduced a new approach to synchronized phasor, frequency, and ROCOF estimation that enables high measurement accuracy also during abrupt variations. It combines the advantages of TFM models in terms of dynamic tracking and disturbance rejection, with the fast response to step events brought by asymmetric TF expansions and recombination.

The simulation results have shown that the proposed approach opens many possibilities to define algorithms capable of dealing with abrupt, unexpected transitions. In particular, its variants can lead to the design of P-class compliant methods like in [27] or M-class solutions as that illustrated here, with remarkable performance in the presence of step changes. Zero or quasi-zero RT can even be obtained under realistic noise conditions and for noninstantaneous changes in the monitored quantity. This makes the proposal very promising to reduce the number of measurements labeled as "bad data" and thus discarded in real-world applications, which is extremely useful for wide area monitoring, protection, and control applications in power systems.

REFERENCES

[1] V. Terzija et al., "Wide-area monitoring, protection, and control of future electric power networks," *Proc. IEEE*, vol. 99, no. 1, pp. 80–93, Jan. 2011.

[2] M. Paolone et al., "Fundamentals of power systems modelling in the presence of converter-interfaced generation," *Electr. Power Syst. Res.*, vol. 189, Dec. 2020, Art. no. 106811.

[3] FERC and NERC. (Apr. 2012). *Arizona-Southern California Outages on September 8, 2011 Causes an Recommendations*. [Online]. Available: https://www.nerc.com/pa/rrm/ea/

[4] AEMO. (Mar. 2017). *Black System South Australia 28 September 2016—Final Report*. [Online]. Available: https://www.aemo.com.au/

[5] G. Rietveld et al., "Measurement infrastructure to support the reliable operation of smart electrical grids," *IEEE Trans. Instrum. Meas.*, vol. 64, no. 6, pp. 1355–1363, Jun. 2015.

[6] L. Zhu et al., "A comprehensive method to mitigate forced oscillations in large interconnected power grids," *IEEE Access*, vol. 9, pp. 22503–22515, 2021.

[7] *IEEE/IEC International Standard—Measuring Relays and Protection Equipment—Part 118-1: Synchrophasor for Power Systems—Measurements*, Standard IEC/IEEE 60255-118-1, Dec. 2018.

[8] A. Derviškadić, P. Romano, and M. Paolone, "Iterative-interpolated DFT for synchrophasor estimation: A single algorithm for P- and M-class compliant PMUs," *IEEE Trans. Instrum. Meas.*, vol. 67, no. 3, pp. 547–558, Mar. 2018.

[9] Y. Wang, C. Lu, I. Kamwa, C. Fang, and P. Ling, "An adaptive filters based PMU algorithm for both steady-state and dynamic conditions in distribution networks," *Int. J. Electr. Power Energy Syst.*, vol. 117, May 2020, Art. no. 105714.

[10] G. Giorgi and C. Narduzzi, "Low-latency phasor measurement using offset time reference and asymmetric dictionary," in *Proc. IEEE 9th Int. Workshop Appl. Meas. Power Syst. (AMPS)*, Sep. 2018, pp. 1–5.

[11] G. Frigo, P. A. Pegoraro, and S. Toscani, "Low-latency, three-phase PMU algorithms: Review and performance comparison," *Appl. Sci.*, vol. 11, no. 5, p. 2261, Mar. 2021.

[12] G. Barchi, D. Macii, D. Belega, and D. Petri, "Performance of synchrophasor estimators in transient conditions: A comparative analysis," *IEEE Trans. Instrum. Meas.*, vol. 62, no. 9, pp. 2410–2418, Sep. 2013.

[13] A. J. Roscoe, A. Dysko, B. Marshall, M. Lee, H. Kirkham, and G. Rietveld, "The case for redefinition of frequency and ROCOF to account for AC power system phase steps," in *Proc. IEEE Int. Workshop Appl. Meas. Power Syst. (AMPS)*, Sep. 2017, pp. 1–6.

[14] P. Castello, M. Lixia, C. Muscas, and P. A. Pegoraro, "Adaptive Taylor–Fourier synchrophasor estimation for fast response to changing conditions," in *Proc. IEEE Int. Instrum. Meas. Technol. Conf.*, May 2012, pp. 294–299.

[15] A. J. Roscoe, "Exploring the relative performance of frequency-tracking and fixed-filter phasor measurement unit algorithms under C37.118 test procedures, the effects of interharmonics, and initial attempts at merging P-class response with M-class filtering," *IEEE Trans. Instrum. Meas.*, vol. 62, no. 8, pp. 2140–2153, Aug. 2013.

[16] P. Castello, J. Liu, C. Muscas, P. A. Pegoraro, F. Ponci, and A. Monti, "A fast and accurate PMU algorithm for P+M class measurement of synchrophasor and frequency," *IEEE Trans. Instrum. Meas.*, vol. 63, no. 12, pp. 2837–2845, Dec. 2014.

[17] M. B. Martins, R. T. D. B. E. Vasconcellos, and P. A. A. Esquef, "Step change detection based on analytic signal for PMU calibrators," in *Proc. IEEE 10th Int. Workshop Appl. Meas. Power Syst. (AMPS)*, Sep. 2019, pp. 1–5.

[18] M. B. Martins, P. A. A. Esquef, and R. T. D. B. E. Vasconcellos, "Enhanced step location in the magnitude and phase of an AC signal via polynomial approximation total variation (PATV) filtering," in *Proc. IEEE 13th Int. Workshop Appl. Meas. Power Syst. (AMPS)*, Sep. 2023, pp. 1–6.

[19] G. Frigo, A. Derviškadić, and M. Paolone, "Reduced leakage synchrophasor estimation: Hilbert transform plus interpolated DFT," *IEEE Trans. Instrum. Meas.*, vol. 68, no. 10, pp. 3468–3483, Oct. 2019.

[20] A. Karpilow, M. Paolone, A. Derviškadic, and G. Frigo, "Step change detection for improved ROCOF evaluation of power system waveforms," in *Proc. Int. Conf. Smart Grid Synchronized Meas. Analytics (SGSMA)*, May 2022, pp. 1–7.

[21] C. Qian and M. Kezunovic, "A novel time-frequency analysis for power system waveforms based on 'pseudo-wavelets,"' in *Proc. IEEE/PES Transmiss. Distribution Conf. Expo.*, Apr. 2018, pp. 1–9.

[22] A. Derviškadic, G. Frigo, and M. Paolone, "Beyond phasors: Modeling of power system signals using the Hilbert transform," *IEEE Trans. Power Syst.*, vol. 35, no. 4, pp. 2971–2980, Jul. 2020.

[23] A. Karpilow, A. Derviškadic, G. Frigo, and M. Paolone, "Characterization of non-stationary signals in electric grids: A functional dictionary approach," *IEEE Trans. Power Syst.*, vol. 37, no. 2, pp. 1126–1138, Mar. 2022.

[24] M. Bertocco, G. Frigo, C. Narduzzi, C. Muscas, and P. A. Pegoraro, "Compressive sensing of a Taylor-Fourier multifrequency model for synchrophasor estimation," *IEEE Trans. Instrum. Meas.*, vol. 64, no. 12, pp. 3274–3283, Dec. 2015.

[25] J. A. de la Serna, "Dynamic phasor estimates for power system oscillations," *IEEE Trans. Instrum. Meas.*, vol. 56, no. 5, pp. 1648–1657, Oct. 2007.

[26] D. Guillen, J. A. D. L. O. Serna, A. Zamora-Méndez, M. R. A. Paternina, and F. Salinas, "Taylor–Fourier filter-bank implemented with O-splines for the detection and classification of faults," *IEEE Trans. Ind. Informat.*, vol. 17, no. 5, pp. 3079–3089, May 2021.

[27] G. Frigo, G. Gallus, P. A. Pegoraro, and S. Toscani, "Improving step performance of PMU algorithms: Left and right Taylor–Fourier expansions," in *Proc. IEEE 13th Int. Workshop Appl. Meas. Power Syst. (AMPS)*, Sep. 2023, pp. 1–6.

[28] M. A. Platas-Garza and J. A. de la Serna, "Dynamic harmonic analysis through Taylor–Fourier transform," *IEEE Trans. Instrum. Meas.*, vol. 60, no. 3, pp. 804–813, Mar. 2011.

[29] M. A. Platas-Garza and J. A. de la Serna, "Dynamic phasor and frequency estimates through maximally flat differentiators," *IEEE Trans. Instrum. Meas.*, vol. 59, no. 7, pp. 1803–1811, Jul. 2010.

[30] D. Belega, D. Fontanelli, and D. Petri, "Dynamic phasor and frequency measurements by an improved Taylor weighted least squares algorithm," *IEEE Trans. Instrum. Meas.*, vol. 64, no. 8, pp. 2165–2178, Aug. 2015.

[31] G. Frigo, P. A. Pegoraro, and S. Toscani, "Enhanced support recovery for PMU measurements based on Taylor–Fourier compressive sensing approach," *IEEE Trans. Instrum. Meas.*, vol. 71, pp. 1–11, 2022.

[32] G. Frigo, A. Derviškadic, Y. Zuo, A. Bach, and M. Paolone, "Taylor–Fourier PMU on a real-time simulator: Design, implementation and characterization," in *Proc. IEEE Milan PowerTech*, Jun. 2019, pp. 1–6.

[33] J. Song, A. Mingotti, J. Zhang, L. Peretto, and H. Wen, "Fast iterative-interpolated DFT phasor estimator considering out-of-band interference," *IEEE Trans. Instrum. Meas.*, vol. 71, pp. 1–14, 2022.

[34] W. Meng, X. Wang, Z. Wang, and I. Kamwa, "Impact of causality on performance of phasor measurement unit algorithms," *IEEE Trans. Power Syst.*, vol. 33, no. 2, pp. 1555–1565, Mar. 2018.

[35] X. Liu, M. Lewandowski, and N. K. C. Nair, "A Morlet wavelet-based two-point FIR filter method for phasor estimation," *IEEE Trans. Instrum. Meas.*, vol. 70, pp. 1–10, 2021.

[36] *IEEE Standard for Synchrophasor Measurements for Power Systems*, Standard IEEE Std C37.118.1-2011, Revision of IEEE Std C37.118-2005, Dec. 2011.

[37] X. Shan, D. Macii, D. Petri, and H. Wen, "Enhanced IpD2FT-based synchrophasor estimation for M class PMUs through adaptive narrowband interferers detection and compensation," *IEEE Trans. Instrum. Meas.*, vol. 73, pp. 1–14, 2024.

[38] S. Toscani, C. Muscas, and P. A. Pegoraro, "Design and performance prediction of space vector-based PMU algorithms," *IEEE Trans. Instrum. Meas.*, vol. 66, no. 3, pp. 394–404, Mar. 2017.

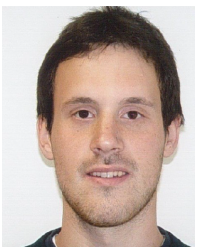

Guglielmo Frigo (Senior Member, IEEE) was born in Padua, Italy, in 1986. He received the B.Sc. and M.Sc. degrees in biomedical engineering from the University of Padova, Padua, in 2008 and 2011, respectively, and the Ph.D. degree from the School of Information Engineering, University of Padova, in 2015, with a dissertation about compressive sensing (CS) theory applications to instrumentation and measurement scenario.

He was a Post-Doctoral Researcher with the Electronic Measurement Research Group, University of Padova, from 2015 to 2017, and the Distributed Electrical Laboratory, Swiss Federal Institute of Technology, Lausanne, Switzerland, from 2018 to 2020. In 2020, he was a Foreign Guest Researcher with the National Institute of Standards and Technology (NIST), Gaithersburg, MD, USA. He is currently a Scientist at METAS, Bern, Switzerland, where he is responsible for the research strategy in energy and mobility. His current research interests include development of enhanced measurement infrastructures for electrical systems.

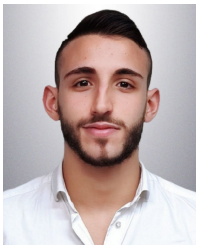

Giacomo Gallus (Graduate Student Member, IEEE) received the M.S. degree (cum laude) in electronic engineering from the University of Cagliari, Cagliari, Italy, in 2021, where he is currently pursuing the Ph.D. degree with the Electrical and Electronic Measurements Group, Department of Electrical and Electronic Engineering.

His research activities focus on synchrophasor measurements, synchronization techniques, and wide area monitoring, protection, and control (WAMPAC) systems.

Paolo Attilio Pegoraro (Senior Member, IEEE) received the M.S. degree (summa cum laude) in telecommunication engineering and the Ph.D. degree in electronic and telecommunication engineering from the University of Padova, Padua, Italy, in 2001 and 2005, respectively.

From 2015 to 2018, he was an Assistant Professor with the Department of Electrical and Electronic Engineering, University of Cagliari, Cagliari, Italy, where he is currently an Associate Professor. He has authored or coauthored more than 150 scientific papers. His current research interests include development of new measurement techniques for modern power networks, with attention to synchronized measurements and state estimation.

Dr. Pegoraro is a member of IEEE IMS TC 39 (Measurements in Power Systems) and IEC TC 38/WG 47. He is an Associate Editor of the IEEE TRANSACTIONS ON INSTRUMENTATION AND MEASUREMENT and the General Chair of the IEEE International Workshop on Applied Measurements for Power Systems (AMPS).

Sergio Toscani (Senior Member, IEEE) received the M.S. and Ph.D. degrees (summa cum laude) in electrical engineering from the Politecnico di Milano, Milan, Italy, in 2007 and 2011, respectively.

From 2011 to 2020, he was an Assistant Professor of electrical and electronic measurement with the Dipartimento di Elettronica, Informazione e Bioingegneria, Politecnico di Milano, where he currently serves as an Associate Professor. His research activity is mainly focused on development and testing of current and voltage transducers, measurement techniques for power systems, electrical components, and systems diagnostics.

Dr. Toscani is a member of the IEEE Instrumentation and Measurement Society and the IEEE TC-39—Measurements in Power Systems.

Open Access funding provided by 'Università degli Studi di Cagliari' within the CRUI CARE Agreement